

Ultrasonic Additive Manufacturing of Metal-Matrix Shape Memory Composites

Ryan Hahnlen, Jennifer L Morris, and Marcelo J Dapino, The Ohio State University, Columbus, OH, United States

© 2021 Elsevier Inc. All rights reserved.

Introduction

Shape memory alloys (SMAs) have unique properties due to a stress- and temperature-dependent phase transformation between martensite, the low-temperature, high-stress phase, and austenite, the high-temperature, low-stress phase. While this transformation is most widely utilized for actuation purposes via the shape memory effect and high-strain components through the pseudoelastic response of initially austenitic alloys, this article investigates the phase-dependent modulus of SMAs and their ability to generate transformation stresses when they are heated in an initially prestrained state. By embedding SMA elements within a metal-matrix composite, changes in elastic modulus allow for stiffness tunability while transformation stresses can create axial loads, both of which result in unique thermomechanical responses.

The specific focus of this article is on the thermally-induced strain response of nickel titanium-aluminum (NiTi-Al) composites. Chief motivation is the development of SMA aluminum-matrix composites with a reduced coefficient of thermal expansion (CTE). This is pursued via the stress developed in the SMA due to phase transformation and strain recovery. By creating a low-CTE, aluminum-based structure, significant weight savings can be realized over traditional low-CTE components based on iron alloys.

Composites in this article are fabricated using ultrasonic additive manufacturing (UAM), a rapid-prototyping technology based on ultrasonic metal welding. In ultrasonic metal welding, two workpieces are held together under a compressive load and ultrasonically vibrated relative to one another. The motion disrupts surface oxides and shears surface asperities, creating nascent surfaces on a microscopic scale (Graff, 2005). The compressive load applied to the pieces causes opposing clean metal surfaces to form metallic bonds, thus joining the two components. During UAM consolidation, illustrated in Fig. 1(a), the ultrasonic vibrations are generated by piezoelectric transducers and transmitted to the workpieces through tuned waveguides and a rolling sonotrode which is specially textured to grip the top workpiece. The primary benefit of UAM is the low process temperatures; pieces are consolidated well below the melting temperature of the participating alloys (Han et al., 2020).

UAM makes it possible to embed within a metal-matrix thermally-sensitive materials such as SMAs, electroactive PVDF, fiber optics, and electronic components (Kong et al., 2004; Chillelli et al., 2019), which would not be possible with other metal-matrix composite technologies that require high process temperatures. During the welding phase, the ultrasonic vibrations and compressive stresses cause plastic deformation of the matrix material. The result is plastic flow of the matrix material around the embedded objects, creating close contact, mechanical interlocking, and possibly solid-state bonding between the composite's components (Yang et al., 2005, 2009; Zhang and Li, 2009). By way of example, fibers ranging from 76 μm , Fig. 1(b), to 381 μm in diameter and ribbons up to 762 μm wide, Fig. 1(c), have been successfully embedded via UAM (Hahnlen and Dapino, 2014).

The key to tailoring thermally-induced strain with SMAs is to prestrain the embedded elements prior to embedding, transforming the twinned martensitic phase to detwinned, or stress-induced, martensite. When constrained and heated in the detwinned martensite phase, SMAs generate a tensile recovery stress, or blocking stress, that is nearly proportional to temperature (Vokoun et al., 2003; Tsoi et al., 2004a; Zak et al., 2003). During this heating cycle, as long as the SMA is perfectly constrained and does not undergo plastic deformation, it will remain in its original detwinned martensitic phase. Creating metal-matrix composites with prestrained SMAs can be challenging as traditional methods such as casting or diffusion-based processes have high temperature periods where the surrounding matrix will not provide enough constraint against the transforming and recovering SMA elements. Being a low-temperature process, UAM is uniquely suited for creating SMA metal-matrix composites as the low temperature prevents transformation and subsequent recovery of prestrain.

Experimental Procedure

Sample Fabrication

Three UAM composites were created to observe the thermomechanical behavior of NiTi-Al UAM systems. In these composites, the NiTi ribbons were heated in an unconstrained state to transform them to austenite and allowed to cool to form twinned martensite. While these composites were not expected to display constrained NiTi behaviors, they were created to characterize the thermoelastic behavior of the composites. In fabricating the composites, two 152 μm thick Al 3003-H18 tapes were first consolidated on an Al 3003-H18 base plate using a 9 kW Fabrisonic UAM system. Rectangular NiTi ribbons, 254 μm by 762 μm , were placed on top of the second tape surface and clamped into position. Two additional Al tapes were consolidated over top of the ribbons to complete the UAM build. The composites were next machined to final dimensions and the base plate removed from the underside of the composites. Composites 1, 2, and 3 have NiTi volume fractions of 5.3%, 15.2%, and 20.6%, respectively.

An additional build, composite 4, was created in a similar manner but with detwinned NiTi ribbons. This composite has a similar volume fraction to composite 2, 15.2%. The NiTi ribbons were detwinned by applying dead weight resulting in a tensile stress of 186 MPa, three times greater than the observed critical finish stress (Stress at which the stress-induced martensitic phase

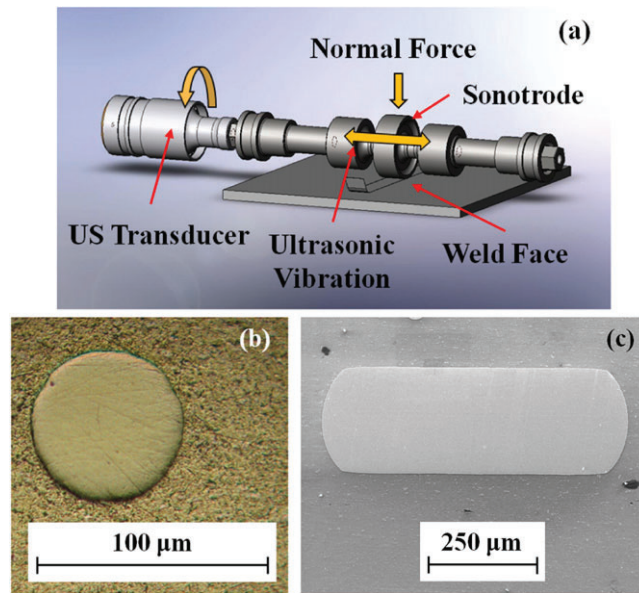


Fig. 1 (a) In the UAM process, successive layers of metal tape are consolidated to create metal composites with seamlessly embedded materials; (b) cross section of a NiTi-Al composite with 76 μm diameter NiTi wire; and (c) 762 μm by 254 μm rectangular NiTi ribbon embedded within an Al matrix.

Table 1 Dimensions and NiTi content of NiTi-Al composites

Composite	Number of Ribbons	Cross-sectional Area [mm^2]	Length [mm]	NiTi Vol. Fraction %
1	1	3.52	76.2	5.3
2	2	2.54	74.0	15.2
3	2	1.88	71.9	20.6
4	2	2.53	57.9	15.2

transformation is complete) of this alloy at room temperature. After design and construction, composite 4 was used for thermally-induced strain characterization. A summary of the composites' characteristics is provided in [Table 1](#).

Thermally-Induced Strain Testing

Thermally-induced strain was measured by heating the composites in a thermal chamber along with an Al 3003-H18 reference sample for three cycles between 25°C and 100°C. During thermal cycles, the strain of both samples was measured with strain gages matched to aluminum alloys, and the temperature was monitored with a thermocouple placed next to each strain gage.

The strain signal from the reference sample was used to remove the thermal dependency of the strain gages from the composite's strain signal. To determine the composite's strain response, the strain measured from the reference sample was subtracted from the strain measured from each composite and the calculated thermal strain of the reference sample was added to the composite's strain measurement ([Lanza di Scalea, 1998](#)):

$$\epsilon_{comp} = \epsilon_{sig/comp} - \epsilon_{sig/ref} + \alpha_{ref} \times \Delta T. \quad (1)$$

Here, $\epsilon_{sig/comp}$ is the non-compensated strain signal from the composite, $\epsilon_{sig/ref}$ is the strain signal from the reference sample, α_{ref} is the CTE of the reference material (23.2 $\mu\text{e}/^\circ\text{C}$ ([Kaufman, 1999](#))), and ΔT is the change in temperature.

Results and Discussion

Thermomechanical Testing

The temperature versus strain plots of composites 1–4 are shown in [Fig. 2\(a\)-\(d\)](#). For each composite, the initial cycle is different than subsequent cycles, however cycles 2 and 3 exhibit stabilized behavior. For clarity, cycles 2 and 3 for each composite are shown in [Fig. 3\(a\)-\(d\)](#) without the initial thermal cycles.

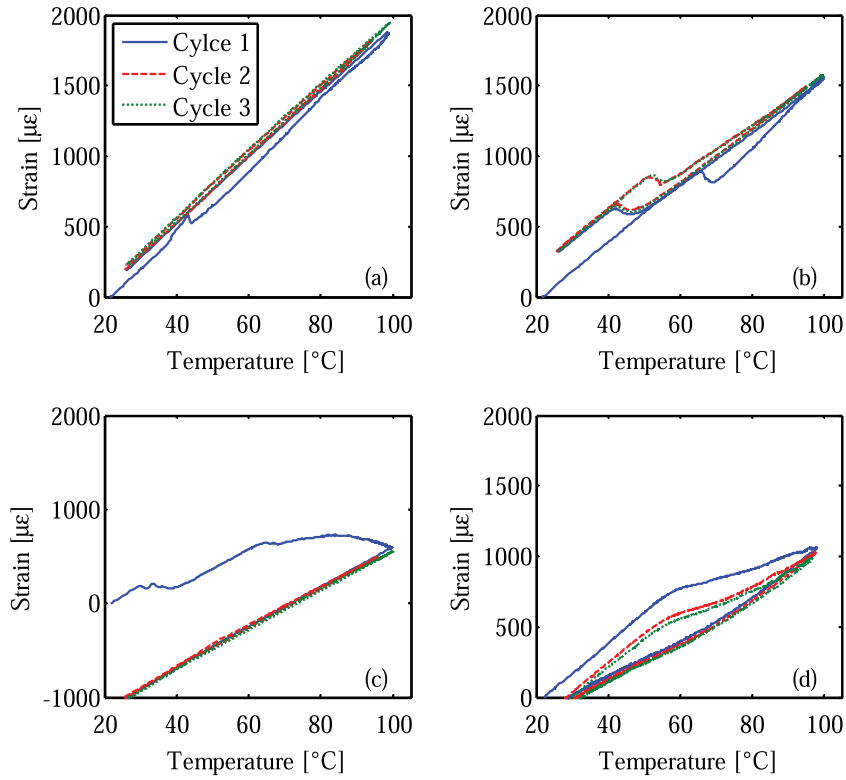


Fig. 2 Temperature versus strain plots for cycles 1 through 3 of NiTi-Al: (a) composite 1; (b) composite 2; (c) composite 3; and (d) composite 4.

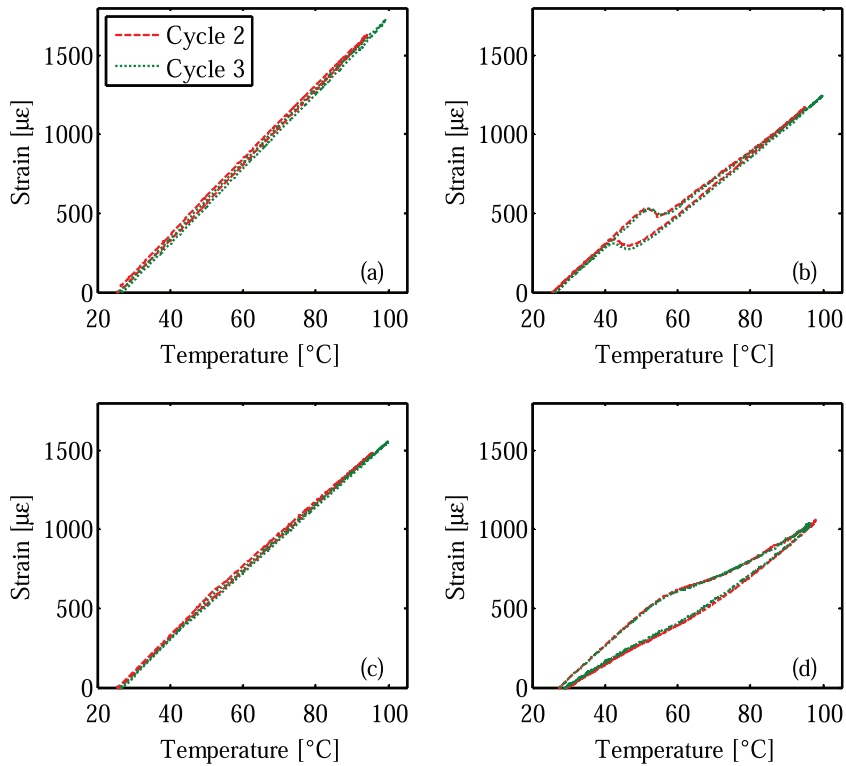


Fig. 3 Temperature versus strain plots for cycles 2 and 3 of NiTi-Al: (a) composite 1; (b) composite 2; (c) composite 3; and (d) composite 4.

Composite 1 has a sudden increase in strain in the initial cycle after which its behavior becomes nearly linear. The spike in the initial cycle, seen at 42°C, is attributed to a stick-slip condition that developed between the ribbon and matrix, allowing the embedded ribbon to contract slightly within the matrix. Under this condition, the matrix exhibits a momentary increase in strain before being constrained again by the NiTi ribbon.

The temperature versus strain behavior of composite 2 is different than that of composite 1. After an initial linear region, the composite recovers some strain as observed by the negative strain-temperature slope seen in Fig. 2(b). After contraction, the composite again behaves linearly with a different CTE than the initial low temperature region. Upon cooling, the process reverses with the exception of a hysteretic recovery of the thermal contraction. The strain recovery suggests that there is some amount of prestrain in the embedded NiTi. Upon heating through the austenite start and finish temperatures, A_s and A_f , the martensite to austenite ($M - A$) transformation recovers the prestrain, causing the observed contraction. Upon cooling, the austenite to martensite ($A - M$) transition occurs over the martensite start and finish temperatures, M_s and M_f , respectively, which produces the observed hysteresis.

The first cycle of composite 2 undergoes the strain contraction over a higher temperature region, approximately 65–70°C, than subsequent cycles. Further, there is a strain offset of approximately 300 $\mu\epsilon$ at the end of the first cycle. The stable behaviors of the second and third cycles have the strain contraction starting at 50°C until approximately 55°C, as observed by the negative strain-temperature slope seen in Figs. 2(b) and 3(b). Through this region, the composite recovers a consistent amount of strain which is then reintroduced upon cooling between 57°C and 52°C. Further cooling results in a thermoelastic strain response bringing the composite back to its original starting strain value. The initial transient behavior seen in the first cycle is attributed to a commonly observed phenomenon with constrained SMAs (Tsoi *et al.*, 2004a,b, 2002). In the initial heating cycle of a prestrained and preloaded SMA, the $M - A$ transformation occurs at higher temperatures due to the applied preload. Upon cooling, the stress decreases linearly to a level below the initial preload. This is due to an intermediate “R-phase” transformation which slightly reduces the amount of stress-induced martensite, allowing the ribbon to reach a lower stress level during cooling. The formation of the R-phase and recovery of prestrain is stable; it occurs only during the first heating cycle and will not occur to a greater extent unless new loading conditions are applied (i.e., higher stresses or temperatures) (Tsoi *et al.*, 2004a; Vokoun *et al.*, 2003). This decrease in stress for subsequent thermal cycles lowers the effective A_s temperature of the SMA embedded within the composite.

Composite 3 has linear behavior similar to composite 1 in its second and third cycles. However, since composite 3 has high a higher NiTi volume fraction than composite 2, a similar response and larger magnitude of strain recovery would be expected. An explanation for the behavior of composite 3 is in the strain response from the initial thermal cycle. In the first cycle, Fig. 2(c), composite 3 exhibits an initial linear region followed by a strain recovery greater in magnitude than composite 2. After this recovery there is a gradual decrease in slope which becomes negative before cooling begins. This gradual slope change and strain recovery are attributed to plastic deformation of the Al matrix from the generation of recovery stresses in the NiTi ribbons.

A prestrained NiTi sample heated under constraint generates a recovery stress that increases with temperature. In being heated to 100°C, the NiTi ribbons in composite 3 appear to generate enough recovery stress to yield the matrix, allowing the ribbons to recover any induced prestrain. This scenario requires that the NiTi ribbons have an initial prestrain, similar to composite 2, as indicated by its hysteretic behavior. In subsequent thermal cycles, composite 3 had no remaining prestrain and therefore behaves in a piecewise fashion with two linear regions.

The behavior of composites 1, 2, and 3 suggests that although steps were taken to embed the NiTi ribbons without prestrain, the NiTi ribbons did experience strain during ultrasonic consolidation. The rolling action of the UAM horn and plastic embedding of the ribbons into the matrix likely induced detwinning of the martensitic structure of the NiTi thus creating a prestrain and non-zero initial stress-induced volume fraction. For composites 1 and 3, the initial heating cycles appear to have removed the initial prestrain through movement of the embedded ribbon in composite 1 or through deformation of the matrix in composite 3.

The first three composites each exhibit two linear regions corresponding to the martensite and austenite phases of the embedded NiTi ribbons. The difference between the slopes of the two linear regions is small in composite 1, however, the effect becomes more pronounced as NiTi fiber volume fraction increases as displayed in the behaviors of composites 2 and 3. Since NiTi has a lower CTE than the Al matrix, the inclusion of NiTi elements will reduce the total composite CTE, α_{comp} , to varying degrees based upon the fiber volume fraction and phase dependent modulus (Clyne and Withers, 1993; Staab, 1999; Schapery, 1968):

$$\alpha_{comp} = \frac{(1 - v)(E_{Al})(\alpha_{Al}) + v(E_{NiTi})(\alpha_{NiTi})}{(1 - v)(E_{Al}) + v(E_{NiTi})}. \quad (2)$$

Here, E_{Al} , E_{NiTi} , α_{Al} , and α_{NiTi} are the elastic moduli and CTEs of Al and NiTi, respectively; v represents the NiTi fiber volume fraction. At high temperatures, the modulus of the embedded NiTi increases, due to transformation to austenite, thus reducing the total composite CTE. This results in a higher strain-temperature slope at low temperatures and a lower slope at high temperatures. A similar, yet less noticeable, effect is the decreasing modulus of the Al matrix with increasing temperature. As the Al modulus decreases, the composite's CTE also decreases.

The strain responses of the three cycles of composite 4, Fig. 3(d), exhibit a hysteretic three-part response. First, the strain increases linearly with temperature like the low-temperature regions present in composites 1–3. At temperatures beyond 54°C, the strain response changes showing a region of significantly lower CTE. This response is due to the generation of blocking stresses in the fully prestrained NiTi ribbons above the effective A_s temperature of the composite. Beyond 70°C, there appears to be the start of a second high temperature linear region that does not fully develop over the temperature range of the conducted thermal cycles.

The second and third cycles of composite 4 are similar to each other, as observed in composites 1–3. The additional cycles are generally similar to the first cycles except for an initial strain offset; in the first cycle, the strain returned to zero at 29°C, indicating that there was strain recovery in the first heating. Similar to cycle 1, at approximately 70°C, the composite appears to enter into a second linear strain region indicating that the recovery region is ending. This is hypothesized to be due to a non-linear blocking behavior. If this behavior is occurring, then the composite may be completing the $M - A$ transformation without recovering all of the induced strain and ceasing to generate additional recovery stress. Without increasing blocking stress with increasing temperature, the composite will exhibit a second thermoelastic region with additional thermally-induced strain governed by the CTE given in Eq. (2).

Composite Modeling

To model the thermal strain response of the composites, a strain matching method, similar to models used for SMA-epoxy composites (Sittner *et al.*, 2002; Sittner and Stalmans, 2000; Sittner *et al.*, 2000), was employed. Under the condition that the interface remains intact, the strain in the fiber direction is identical for the Al matrix and NiTi ribbons. Further conditions include consideration of only elastic and transformation-based strains and reversible transformation upon cooling; the model applies only to the stabilized thermal cycles for each composite. The Al and NiTi strains can be expanded into their constituent components for mechanical, thermal, and transformation strain, as applicable:

$$\varepsilon_{Al} = \frac{1}{E_{Al}} (\Delta\sigma_{Al}) + \alpha_{Al}(\Delta T) \quad (3)$$

and

$$\varepsilon_{NiTi} = \frac{1}{E_{NiTi}} (\Delta\sigma_{NiTi}) + \alpha_{NiTi}(\Delta T) + \varepsilon_L(\xi_s - \xi_{so}), \quad (4)$$

where $\Delta\sigma$ is the change in total stress from the initial state, ξ_s is the stress-induced martensitic volume fraction, ξ_{so} is the initial stress-induced martensitic volume fraction, and ε_L is the maximum recoverable strain of NiTi.

In the thermally-induced strain tests, no external load is applied; the composite is allowed to freely expand or contract as the temperature changes. As such, force balancing is used to obtain the stress in the Al matrix in terms of the NiTi stress:

$$\begin{aligned} \sigma_{NiTi} A_{NiTi} + \sigma_{Al} A_{Al} &= 0 \\ \sigma_{Al} &= -\frac{A_{NiTi}}{A_{Al}} \sigma_{NiTi} \\ \sigma_{Al} &= \frac{-v}{(1-v)} \sigma_{NiTi}, \end{aligned} \quad (5)$$

where A_{NiTi} and A_{Al} are the cross sectional areas of the NiTi ribbons and Al matrix, respectively. The variable change from cross sectional area to fiber volume fraction can be made because the NiTi ribbons provide long-fiber reinforcement of the Al matrix, making the lengths of both components equal, $L_{NiTi} = L_{Al}$. Assuming zero initial stress, the stress in the ribbons can be obtained as a function of temperature, material properties, volume fraction, and NiTi transformation terms by substituting Eq. (5) into Eq. (3), equating to Eq. (4), and solving for σ_{NiTi} :

$$\sigma_{NiTi} = \frac{(\alpha_{Al} - \alpha_{NiTi})(\Delta T)}{\frac{1}{E_{NiTi}} + \frac{1}{E_{Al}} \frac{v}{(1-v)}} - \frac{\varepsilon_L(\xi_s - \xi_{so})}{\frac{1}{E_{NiTi}} + \frac{1}{E_{Al}} \frac{v}{(1-v)}}. \quad (6)$$

This equation has two components: the first is the thermoelastic component which any composite exhibits if a CTE mismatch exists between the fibers and matrix; the second is due to the transformation-induced strain recovery of NiTi if it is embedded in a detwinned state ($\xi_{so} \neq 0$). If the embedded NiTi elements are not prestrained before fabrication, only the thermoelastic stress component remains but this component is nonlinear due to the change in modulus as the NiTi ribbons transform between martensite and austenite. Once the NiTi stress is calculated, it can be used in Eq. (4) to determine total composite strain:

$$\varepsilon_{comp} = \frac{1}{E_{NiTi}} \left[\frac{(\alpha_{Al} - \alpha_{NiTi})(\Delta T)}{\frac{1}{E_{NiTi}} + \frac{1}{E_{Al}} \frac{v}{(1-v)}} - \frac{\varepsilon_L(\xi_s - \xi_{so})}{\frac{1}{E_{NiTi}} + \frac{1}{E_{Al}} \frac{v}{(1-v)}} \right] + \alpha_{NiTi}(\Delta T) + \varepsilon_L(\xi_s - \xi_{so}). \quad (7)$$

The same result is obtained by calculating the Al stress and using it in Eq. (3).

For simplicity, composites 1–3 are assumed to be consolidated in a twinned martensite state, having an initial stress-induced volume fraction of zero. As such, the initial models for thermally-induced strain do not include the transformation strain recovery components and Eq. (7) becomes:

$$\varepsilon_{comp} = \frac{1}{E_{NiTi}} \left[\frac{(\alpha_{Al} - \alpha_{NiTi})(\Delta T)}{\frac{1}{E_{NiTi}} + \frac{1}{E_{Al}} \frac{v}{(1-v)}} \right] + \alpha_{NiTi}(\Delta T). \quad (8)$$

Table 2 Material properties used in the composite model presented here. Unless cited, values were found experimentally

Property	Description	Value
$E_A(24^\circ\text{C})$ (Kaufman, 1999)	Al 3003 modulus, 24°C	68.3 GPa
$E_A(100^\circ\text{C})$ (Kaufman, 1999)	Al 3003 modulus, 100°C	65.5 GPa
α_{Al} (Kaufman, 1999)	Al 3003 CTE	$23.2 \mu\text{e}/^\circ\text{C}$
E_A (Matthey, 2012)	Austenite modulus	83 GPa
E_M	Martensite modulus	17.9 GPa
α_{NiTi} (Lagoudas, 2008)	NiTi CTE	$10 \mu\text{e}/^\circ\text{C}$
M_f	Martensite finish temp.	41°C
M_s	Martensite start temp.	45°C
A_s	Austenite start temp.	45°C
A_f	Austenite finish temp.	60°C
C_M	Martensite stress influence coefficient	8.1 MPa/ $^\circ\text{C}$
C_A	Austenite stress influence coefficient	8.2 MPa/ $^\circ\text{C}$
ε_L	Maximum recovery strain	-6.0%

The strain calculation is completed by finding the elastic modulus of the NiTi ribbons as a function of martensitic volume fraction and the Al matrix as a function of temperature. The elastic modulus of the Al matrix is varied linearly using modulus values at different temperatures as found in the literature (Kaufman, 1999). The elastic modulus of NiTi is found through a rule of mixtures calculation between its martensite and austenite phases:

$$E_{NiTi} = E_A + \xi(E_M - E_A) \quad (9)$$

where E_A and E_M are the elastic moduli of austenite and martensite, respectively, and ξ is the total martensitic volume fraction. The martensitic volume fraction only decreases over the range defined by the austenite start and finish temperatures as composite temperature increases. Conversely, martensitic volume fraction only increases over the martensitic start and finish temperatures while the composite temperature is decreasing. For the NiTi ribbons used in this study, the transition temperatures were found through electrical resistance tests and DSC as shown in Table 2 along with other experimentally derived material properties. Even in the thermoelastic case, the increasing NiTi stress due to thermal mismatch of the NiTi ribbons and Al matrix necessitates using the stress-modified transformation temperatures, which are assumed to vary linearly with stress (Liang and Rogers, 1990, 1997; Lagoudas, 2008). In the case of an initial stress-induced martensitic volume fraction ($\xi_{s0} \neq 0$), the transformation temperatures will increase further due to additional stresses generated from SMA strain recovery.

The martensitic volume fractions are found through equations based upon the Liang and Rogers constitutive SMA models (Liang and Rogers, 1990, 1997). For the $M - A$ transformation, the volume fraction is:

$$\xi = \frac{\xi_0}{2} \{ \cos[a_A(T - A_s^\sigma)] + 1 \}, \quad (10)$$

where

$$a_A = \frac{\pi}{A_f - A_s} \quad (11)$$

and

$$A_s^\sigma = A_s + \frac{\sigma}{C_A}. \quad (12)$$

For the $A - M$ transformation, the total volume fraction is calculated using:

$$\xi = \frac{1 - \xi_0}{2} \cos[a_M(T - M_f^\sigma)] + \frac{1 + \xi_0}{2}, \quad (13)$$

where

$$a_M = \frac{\pi}{M_s - M_f} \quad (14)$$

and

$$M_f^\sigma = M_f + \sigma_{NiTi}/C_M \quad (15)$$

where C_M and C_A are the stress influence coefficients for the martensitic and austenitic temperatures, respectively. The total initial martensite volume fraction is denoted ξ_0 .

The thermally-induced strains were modeled for each composite using the material properties for the Al matrix and NiTi ribbons given in Table 2. The model output can be seen for composites 1–3 in Fig. 4(a)–(c), respectively. For composites 1 and 3 the strain model closely matches the strain observed in the second and third thermal cycles of the experiments, including unique high and low temperature linear regions and a small amount of hysteresis. However, the model does not describe the negative

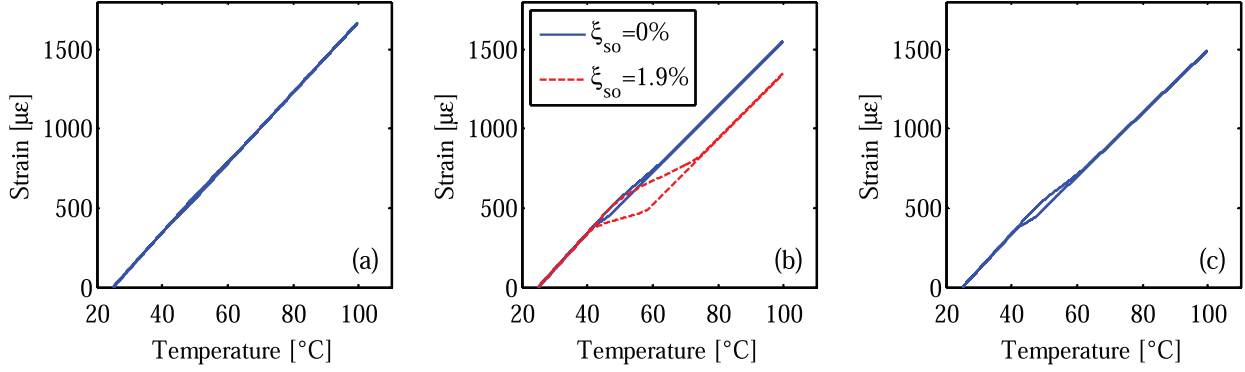


Fig. 4 Thermally-induced strain models for NiTi-Al: (a) composite 1; (b) composite 2; and (c) composite 3.

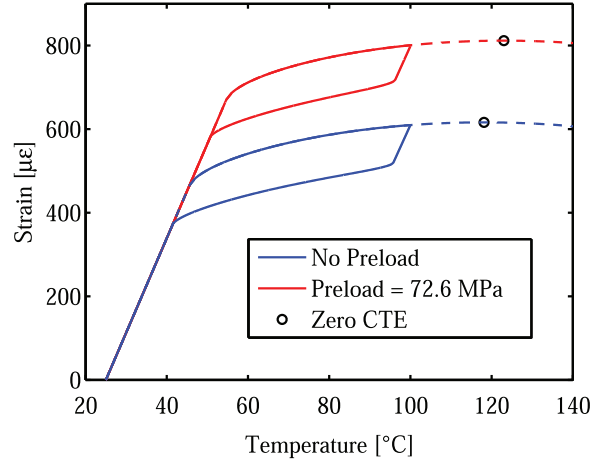


Fig. 5 Modeled thermally-induced strain for composite 4 showing the effect of prestress on the embedded NiTi ribbons.

strain-temperature regions observed in composite 2. This confirms that the zero prestrain assumption is not valid when considering composite 2, and there is residual prestrain that was induced by the rolling action of the sonotrode during fabrication that persists after thermal cycling. The amount of prestrain and subsequent stress-induced martensite is determined by observing the amount of strain recovered as the NiTi ribbons go through the $M - A$ transformation.

The strain recovery region observed in composite 2 is consistent over multiple cycles. Because of this, the transformation is assumed to recover and induce a repeatable amount of stress-induced martensite (Brinson, 1993) as the composite is heated and cooled. To this end, an assumption is made that $\xi_s = \xi_{so} \times \xi$ where ξ is found from Eq. (10) and Eq. (13) for purposes of calculating composite strain. Here, ξ_s denotes stress-induced martensite volume fraction and ξ_{so} is the initial stress-induced martensite volume fraction. By taking the average strain of the rising and falling high temperature linear regions at $T = 65^\circ\text{C}$, a temperature slightly beyond the $M - A$ transformation region, and subtracting the modeled thermoelastic strain for composite 2 at 65°C , the total composite recovery strain, $\varepsilon_{\text{NiTi}/X}$, is estimated to be $200 \mu\epsilon$. To calculate the initial stress-induced volume fraction from the total observed strain recovery, the thermoelastic strain component from Eq. (8) is subtracted from the total strain from Eq. (7),

$$\varepsilon_{\text{NiTi}/X} = \frac{1}{E_{\text{NiTi}}} (\sigma_{\text{NiTi}/X}) + \varepsilon_L (\xi_s - \xi_{so}), \quad (16)$$

where $\sigma_{\text{NiTi}/X}$ is equal to the second term of Eq. (6). Considering $E_{\text{NiTi}} = E_A$ and $\xi_s = 0$ when the $M - A$ transformation is complete,

$$\begin{aligned} \varepsilon_{\text{NiTi}/X} &= \frac{1}{E_{\text{NiTi}}} \left[\frac{-\varepsilon_L (\xi_s - \xi_{so})}{\frac{1}{E_{\text{NiTi}}} + \frac{1}{E_A (1-v)}} \right] + \varepsilon_L (\xi_s - \xi_{so}) \\ &= -\varepsilon_L \xi_{so} \left[1 - \frac{1}{1 + \frac{E_A}{E_{\text{NiTi}}} v} \right]. \end{aligned} \quad (17)$$

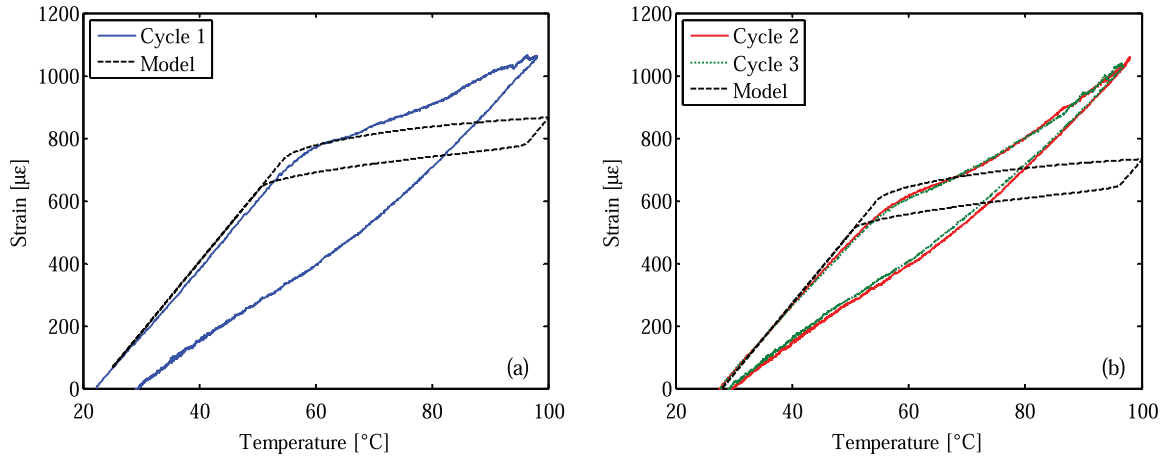


Fig. 6 Thermally-induced strain model compared to thermally-induced strain data for composite 4: (a) cycle 1 and (b) cycles 2 and 3.

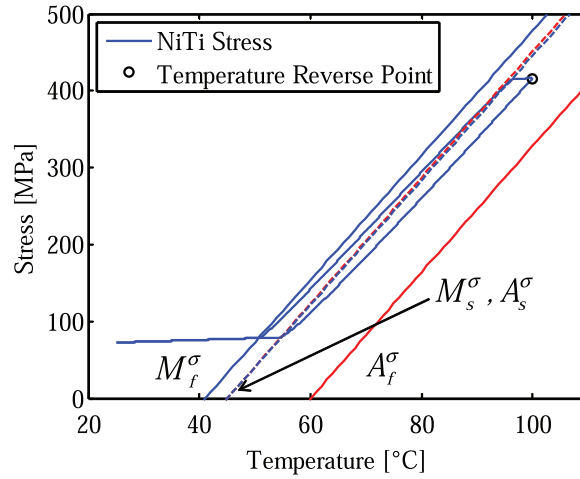


Fig. 7 Modeled stress-temperature load path of NiTi in composite 4 during heating, partial transformation, and cooling overlaid on the NiTi phase diagram. At 100°C, the location between the A_s^σ and A_f^σ lines correspond to a martensitic volume fraction of 0.81.

Using 200 $\mu\epsilon$ for $\epsilon_{NiTi/X}$, the initial stress-induced martensitic volume fraction is found to be 1.9%. With the calculated value for ξ_{50} used in Eq. (7), the dashed line in Fig. 4(b) shows the thermally-induced strain model for composite 2 including the transformation strain component. With the inclusion of the transformation strain term, the model closely matches the experimental data and exhibits the expanded hysteretic region originally observed.

Using the strain modeling techniques used to describe composites 1–3, the behavior of composite 4 was modeled prior to testing using a volume fraction of 15.2%. The resulting thermally-induced strain model is shown in Fig. 5. The linear thermoelastic region was predicted to end at an A_s^σ temperature of 45.6°C followed by a region of continuously decreasing CTE. The modeled behavior is extrapolated beyond the expected 100°C maximum temperature, exhibiting a zero CTE at 118°C.

As compared to the thermally-induced strain data given in Figs. 2(d) and 3(d), effective austenite start temperatures, A_s^σ , at the end of the thermoelastic response occur at 57.7°C, 54.7°C, and 54.4°C for the first, second, and third cycles, respectively. The decrease in A_s^σ can be attributed to a tensile load applied to the ribbons during the embedding process, similar to those observed in the initial heating responses of composites 1–3. Using Eq. (12) and the results from the steady-state behavior observed in cycles 2 and 3, the axial preload on the ribbons due to embedding is estimated to be 72.6 MPa. Using this preload and the NiTi fiber volume fraction of 15.2%, the model is compared to the thermally-induced strain data for composite 4 in Fig. 6.

The thermally-induced strain model and data are in close agreement until approximately 70°C, where the composite appears to progress further through the $M - A$ transformation. This was not expected as even a modeled stress-temperature load path of the NiTi ribbon within the composite, Fig. 7, shows a martensitic volume fraction of 0.81 at 100°C, corresponding to only a 19% transformation. Fig. 7 plots the stress in the NiTi ribbon as calculated through Eq. (6) as a function of composite temperature. There is an initial thermoelastic increase in stress until A_s^σ , at which point increases in transformation stresses are generated for further increases in temperature. The compliance of the Al matrix allows a small fraction of NiTi to transform to austenite with

Table 3 Comparison of experimentally observed strain at maximum temperature and modeled strain for composites 1–4. The parenthetical value for composite 2 corresponds to the model with $\xi_{so} = 1.9\%$

Composite	Max. temp. [°C]	Exp. strain [$\mu\epsilon$]	Modeled strain [$\mu\epsilon$]
1	99	1720	1653
2	100	1244	1549 (1327)
3	100	1560	1495
4	98	1059	742

Table 4 Material properties for NiTi pseudoelastic ribbons used in composite model. Unless cited, values were found experimentally

Property	Description	Value
E_A (Nitinol Devices & Components, 2012)	Austenite modulus	75 GPa
E_M (Nitinol Devices & Components, 2012)	Martensite modulus	41 GPa
α_{NiTi} (Lagoudas, 2008)	NiTi CTE	10 $\mu\epsilon/^\circ\text{C}$
M_f	Martensite finish temp.	−78°C
M_s	Martensite start temp.	−55°C
A_s	Austenite start temp.	16°C
A_f	Austenite finish temp.	18°C
C_M	Martensite stress influence coeff.	3.6 MPa/°C
C_A	Austenite stress influence coeff.	7.4 MPa/°C
ϵ_L	Maximum recovery strain	−6.3%

increasing temperature. When the temperature reverses at 100°C there is an initial thermoelastic response until the load path intersects the M_s^c line. As temperatures continue to cool, the $A - M$ transformation reduces the stress in the NiTi as any austenite is transformed back to detwinned martensite. Transformation is complete at M_f^c and further reduction in temperature produces a thermoelastic response.

Two hypotheses are put forth to describe the deviation between the modeled and experimentally observed behavior. First, there may be a strain gradient through the thickness of the composite, allowing the SMA to contract further than predicted or observed by the surface mounted strain gages. However, since the composite is relatively thin, this strain gradient is not likely to be large. Second, high-temperature, high-stress blocking behavior of the SMA may start to deviate from the behavior portrayed in Fig. 7 at temperatures above 70°C. If the blocking stress generated by the NiTi ribbon begins to reach a steady value, thermoelastic behavior of the composite will continue as the blocking stress no longer increases. If the transformation is able to complete at lower stress levels, this would result in additional hysteresis as there would be a larger thermoelastic response upon cooling prior to reaching the M_s^c temperature.

A summary comparison of the maximum strains observed in the composites at their respective maximum temperatures and the model output at each respective temperature is shown in Table 3. For low prestrain composites, the model results match well with experimental results. Due to the deviation from linear blocked behavior of NiTi, composite 4 exhibits a significant discrepancy between the calculated and experimental results.

Thermally-Invariant Composite

While in practice composite 4 will likely not attain a zero CTE behavior as described by the model, the lowest CTE found through linear interpolation of the transformation regions is 4.9 $\mu\epsilon/^\circ\text{C}$ in the blocking region of cycle 1. If only the repeatable cycles 2 and 3 are considered, the average CTE in the blocking region is 7.6 $\mu\epsilon/^\circ\text{C}$, over a 2/3 reduction compared to the CTE of the Al 3003 matrix. With the results observed in these experiments, some considerations for future composites are given to obtain zero CTE behavior. While composite 4 begins to deviate from the linear blocked behavior at higher temperatures, it is believed that this can be avoided if the blocking behavior can be utilized at lower temperatures and stresses. By using a detwinned pseudoelastic alloy, the beginning of the blocking behavior can be made to occur at a lower temperature due to the inherently lower A_s values of pseudoelastic alloys. A pseudoelastic alloy has been characterized, properties provided in Table 4, in preparation for the next series of composites. This alloy demonstrates the immediate generation of blocking stress upon heating beyond room temperature when prestrained and constrained. The immediate generation of blocking stress effectively removes the linear thermoelastic region as observed in composite 4 below 54°C. A model of thermally-induced strain for a hypothetical composite made with this pseudoelastic ribbon is compared to a similar composite made with shape memory ribbon in Fig. 8.

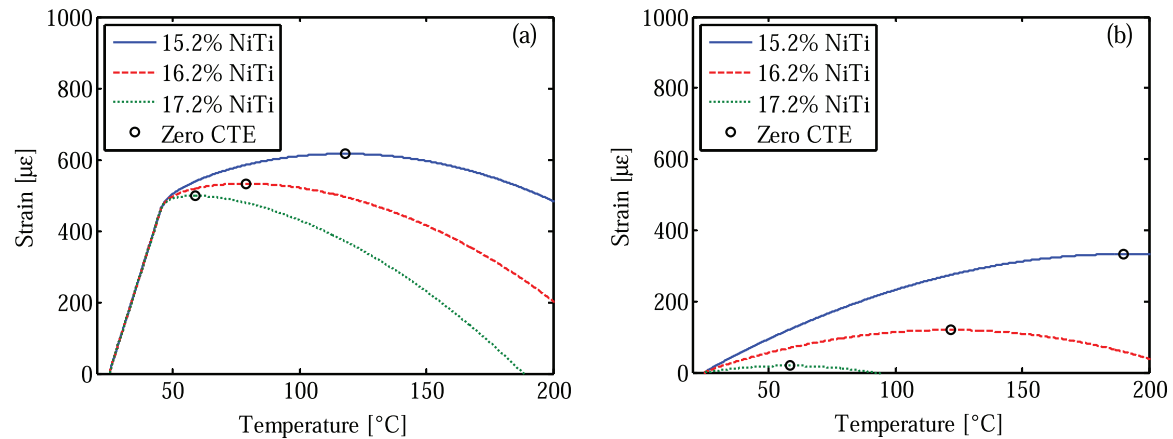


Fig. 8 Comparison of modeled thermally-induced strain for different fiber volume fractions of a composite constructed with (a) shape memory and (b) pseudoelastic alloys.

In addition to lowering the transformation temperatures in the embedded NiTi ribbons, the composite's CTE behavior can be adjusted by increasing the NiTi fiber volume fraction. Small increases in the volume fraction cause the zero CTE behavior to occur at lower temperatures, as shown in Fig. 8(a) for a composite similar to composite 4 and Fig. 8(b) for a composite made with the pseudoelastic NiTi. While increasing the volume fraction does cause the zero CTE point to occur at lower temperatures, it also hastens the occurrence of the negative CTE region. A composite that contracts upon heating is useful for actuation purposes, however it may be as undesirable depending upon the design conditions. The effect of prestress on the NiTi ribbons is also detrimental to achieving a zero CTE. The axial load effectively increases the temperature at which the blocking stresses are generated, allowing the linear thermal expansion region of the composite to further increase the total strain after the stress-free austenite start temperature. The estimated preload on composite 4 also causes the zero CTE point to occur at a higher temperature, 123°C versus 118°C, as shown in Fig. 5. Due to the UAM process, it is not likely that prestress will ever be fully removed, hence its effect on ribbons needs to be quantified so it can be accounted for in composite design.

Utilizing the same procedure as used for composites 1–4, an additional composite has been fabricated with 178 μm by 356 μm embedded NiTi ribbons. Prior to embedding, the ribbons were detwinned by applying a dead weight, similar to the ribbons used in composite 4. The composite was machined to have a NiTi volume fraction of 17.2%. By further increasing the NiTi fiber volume fraction, the temperature at which zero CTE is attained and the total composite strain are both reduced regardless of the NiTi alloy used, as shown in Fig. 8. According to model prediction, the thermally-induced strain behavior of a composite with 17.2% pseudoelastic NiTi by volume will follow the dotted line in Fig. 8(b) with a zero CTE point at 55°C. In using a pseudoelastic alloy and designing the composite with a lower zero CTE temperature, the stress in the NiTi ribbons at the zero CTE temperature are significantly lower than in the shape memory ribbons. This will avoid the high-temperature, high-stress region that is the primary source of discrepancy between the current model and the thermally-induced strain behavior exhibited by composite 4.

Summary

The thermally-induced strain behavior of four NiTi-Al UAM composites was experimentally characterized and modeled. The composites have different fiber volume fractions of NiTi and different levels of initial stress-induced martensite or NiTi prestrain. Two primary regimes are observed. The first is the variable thermoelastic strain behavior where the composites exhibit a linear increase in strain with increasing temperature. In this regime, the NiTi ribbons provide different levels of constraint against the thermal expansion of the Al matrix depending upon their phase. At low temperatures, the constraint is relatively minor due to the low modulus of martensite while, at high temperatures, the lower modulus of the Al matrix and increased modulus of the austenitic NiTi ribbons provide a greater restraint against the Al thermal expansion, leading to a reduced linear CTE of the composite. The effect of the NiTi ribbons is dependent upon the fiber volume fraction: more NiTi fiber volume results in a larger constraint and larger change in CTE.

The second regime in thermally-induced strain behavior is due to a non-zero initial stress-induced martensite volume fraction. As the temperature increases, the NiTi ribbons begin to undergo a $M - A$ transformation which recovers strain induced through the stress-induced transformation to detwinned martensite. If this recovery is inhibited, a temperature-dependent recovery stress is generated by the NiTi elements. In the case of composites 2 and 4, the stress-induced martensite created regions over which the composite has a significantly reduced CTE. At the minimum, composite 4 exhibits a CTE of $7.6 \mu\text{ε}/^\circ\text{C}$, more than a two-thirds reduction relative to the CTE of the Al matrix. Using the developed composite model and properties obtained from characterization

of a pseudoelastic NiTi alloy, a design has been created for a composite with a blocked strain behavior near room temperature, eliminating the initial thermoelastic response of composites 1–4.

The composite model was developed based upon bivariate constitutive SMA and phenomenological SMA composite frameworks from the literature. The SMA model is used to create a strain-matching framework to describe the thermomechanical behavior of an SMA composite. The total composite model is dependent only on material properties, fiber volume fraction, and SMA prestrain level and closely matches the thermally-induced strain data for composites 1–3. The model for composite 4 matches well up to approximately 70°C, at which point, the assumed linear relationship between stress and temperature of the blocked ribbons begins to become inaccurate. Further, the high temperature behavior of composite 4 suggests that the $M - A$ transformation is nearly complete at 100°C, an unexpected result. Further study is required on the behavior of the SMA ribbons at high stresses and temperatures to improve upon the current model. The model was used to design a composite with pseudoelastic NiTi ribbons, currently under construction, that will exhibit zero CTE behavior at 55°C without the thermoelastic behavior observed in composites with shape memory NiTi.

Both the experimental and modeling results show that it is possible to develop a lightweight structure with a tailored CTE. Such structures could be designed to match CTEs in multi-material systems to avoid thermal stresses or to create thermally-invariant structures that provide a significant weight savings over traditional iron-based low CTE alloys. Further, if the SMA volume fraction and initial stress-induced martensitic volume fraction are sufficiently high, it is possible to create components with a negative CTE to achieve structures that exhibit solid-state actuation. The work presented represents a construction and development methodology that can be utilized to create such adaptable structures.

Acknowledgment

Financial support was provided by the member organizations of the Smart Vehicle Concepts Center, a Phase III National Science Foundation Industry-University Cooperative Research Center (www.SmartVehicleCenter.org) under Grant NSF IIP1738723.

References

- Brinson, L., 1993. One dimensional constitutive behavior of shape memory alloys. *Journal of Intelligent Material Systems and Structures* 4 (2), 229–242.
- Chilelli, S.K., Schomer, J.J., Dapino, M.J., 2019. Detection of crack initiation and growth using fiber Bragg grating sensors embedded into metal structures through ultrasonic additive manufacturing. *MDPI Sensors* 19 (22).
- Clyne, T., Withers, P., 1993. *An Introduction to Metal Matrix Composites*. Cambridge: Cambridge University Press, pp. 12–14.
- Graff, K., 2005. Chapter 9 – Ultrasonic metal welding. In: Ahmed, N. (Ed.), *New Developments in Advanced Welding*. Cambridge: Woodhead Publishing Limited, pp. 241–269.
- Hahnlen, R., Dapino, M.J., 2014. NiTi-Al interface strength in ultrasonic additive manufacturing composites. *Composites Part B Engineering* 59, 101–108.
- Han, T., Kuo, C.-H., Sridharan, N., *et al.*, 2020. Effect of weld power and interfacial temperature on mechanical strength and microstructure of carbon steel 4130 fabricated by ultrasonic additive manufacturing. *Manufacturing Letters* 25, 64–69.
- Matthey, J., 2012. Nitinol technical specifications: Transformation, physical, electrical, magnetic and mechanical, Available at: <http://jmmmedical.com/index.php?p=resources&id=221>.
- Kaufman, J. (Ed.), 1999. *Properties of Aluminum Alloys: Tensile, Creep, and Fatigue Data at High and Low Temperatures*. OH: The Aluminum Association, Inc. and ASM International, Materials Park, p. 100.
- Kong, C., Soar, R., Dickens, P., 2004. Ultrasonic consolidation for embedding SMA fibres within aluminium matrices. *Composite Structures* 66, 421–427.
- Lagoudas, D.C., 2008. *Shape Memory Alloys*. New York, NY: Science and Business Media, LLC, pp. 53–119.
- Lanza di Scalea, F., 1998. Measurement of thermal expansion coefficients of composites using strain gauges. *Experimental Mechanics* 328 (4), 233–241.
- Liang, C., Rogers, C.A., 1990. One-dimensional thermomechanical constitutive relations for shape memory materials. *Journal of Intelligent Material Systems and Structures* 1, 207–234.
- Liang, C., Rogers, C.A., 1997. One-dimensional thermomechanical constitutive relations for shape memory materials. *Journal of Intelligent Material Systems and Structures* 8, 285–302.
- Nitinol Devices & Components 2012. Material data sheet: Superelastic Nitinol alloys, Available at: <http://www.nitinol.com/wp-content/uploads/2012/01/Material-Data-Sheet-Superelastic.pdf>.
- Schapery, R.A., 1968. Thermal expansion coefficients of composite materials based on energy principles. *Journal of Composite Materials* 2 (3), 380–404.
- Sittner, P., Stalmans, R., 2000. Developing hybrid polymer composites with embedded shape-memory alloy wires. *JOM* 52 (10), 15–20.
- Sittner, P., Stalmans, R., Tokuda, M., 2000. An algorithm for prediction of the hysteretic responses of shape memory alloys. *Smart Materials and Structures* 9 (4), 452–465.
- Sittner, P., Michaud, V., Schrooten, J., 2002. Modeling and material design of SMA polymer composites. *Materials Transactions* 43 (5), 984–993.
- Staab, G., 1999. *Laminar Composites*. Boston, MA: Butterworth-Heinemann, p. 91.
- Tsoi, K.A., Stalmans, R., Schrooten, J., 2002. Transformational behavior of constrained shape memory alloys. *Acta Materialia* 50, 3535–3544.
- Tsoi, K.A., Schrooten, J., Zheng, Y., Stalmans, R., 2004a. Part I. Thermomechanical characteristics of shape memory alloys. *Materials Science and Engineering A* 368, 286–298.
- Tsoi, K.A., Schrooten, J., Zheng, Y., Stalmans, R., 2004b. Part II. Thermomechanical characteristics of shape memory alloy composites. *Materials Science and Engineering A* 368, 299–310.
- Vokoun, D., Kafka, V., Hu, C., 2003. Recovery stresses generated by NiTi shape memory wires under different constrain conditions. *Smart Materials and Structures* 12, 680–685.
- Yang, Y., Ram, G.D.J., Stucker, B.E., 2005. Enhanced diffusion and phase transformation during ultrasonic welding of zinc and aluminum. *Scripta Materialia* 52, 939–943.
- Yang, Y., Ram, G.D.J., Stucker, B.E., 2009. Bond formation and fiber embedment during ultrasonic consolidation. *Journal of Material Processing Technology* 209, 4915–4924.
- Zak, A.J., Carlmell, M.P., Ostachowicz, W.M., Wiercigroch, M., 2003. One-dimensional shape memory alloy models for use with reinforced composite structures. *Smart Materials and Structures* 12, 338–346.
- Zhang, C., Li, L., 2009. A coupled thermal-mechanical analysis of ultrasonic bonding mechanism. *Metallurgical and Materials Transactions B* 40B, 196–207.